Interoperability of SeaSondes and Wellen Radars in Mapping Radial Surface Currents

J. MARTINEZ-PEDRAJA AND L. K. SHAY

Division of Meteorology and Physical Oceanography, Rosenstiel School of Marine and Atmospheric Science, University of Miami, Miami, Florida

B. K. HAUS

Division of Applied Marine Physics, Rosenstiel School of Marine and Atmospheric Science, University of Miami, Miami, Florida

C. WHELAN

CODAR Ocean Sensor, Mountain View, California

(Manuscript received 28 January 2013, in final form 25 June 2013)

ABSTRACT

A dual-station high-frequency (HF) Wellen Radar (WERA) transmitting at 16 MHz has observed near-real-time surface currents over an approximate range of 100 km across the Florida Straits since July 2004. During a 10-day period in April 2005 (15–25 April), a pair of 12.6-MHz SeaSondes (SS) were deployed south of the WERAs sites by NOAA's Center for Operational Oceanographic Products and Services (CO-OPS). The resulting SS grid overlapped the southern portion of the WERA domain. During the same period of time, a bottom-mounted acoustic Doppler current profiler (ADCP) acquired subsurface current measurements within these HF radar grids starting at 14 m below the surface in water of 86-m depth. The interoperability of beam-forming (WERA) and direction-finding (SS) HF radar technologies was examined. Comparisons of radial and vector currents for an 8-day concurrent time series suggested good agreement in current direction over both domains, where the surface currents' magnitudes were a maximum of 1.2 m s^{-1}. In the core of the radar domains consisting of 108 cells, hourly vector currents were obtained by combining WERA and SS radials. Generally, this can be done in a relatively straightforward manner, considering the geometric dilution of precision (GDOP). A second key issue is downscaling the SS measurements from a 3-km grid to a 1.1-km grid to match the WERA output. This enhanced grid spacing is important along the western flank of the Florida Current, where energetic, small-scale surface features have been observed.

1. Introduction

High-frequency (HF) electromagnetic signals propagate in ground wave modes over the conductive ocean's surface to map radial surface currents using the concept of Bragg scattering (Crombie 1955; Stewart and Joy 1974; Barrick et al. 1977; Paduan and Graber 1997). Briefly, Bragg scattering by an incident electromagnetic wave is associated with a surface gravity wavelength of one-half that of the transmitted wave. The received signal's frequency will be Doppler shifted from the transmitted frequency because of the phase speed of the surface wave and the magnitude of the radial surface current relative to the radar site. In the absence of currents, the Doppler positions of these peaks are at the Bragg frequency as per the dispersion relationship. Moreover, a single radar site provides surface current measurements in both radial directions, either moving toward or away from the radar at a given bearing and range. Thus, radial currents from two or more sites are required to calculate two-dimensional vector currents.

All HF radars resolve the range to the target with precision; however, the bearing angle to the scattering point is more difficult to estimate. Uncertainties in mapping surface currents are partially due to limitations determining these bearings. Currently, there are two types of HF radars in broad use today that resolve bearing angles in different ways: phased arrays such as the Wellen Radar (WERA) and compact directional antennas

Corresponding author address: Jorge Martinez-Pedraja, MPO, Rosenstiel School of Marine and Atmospheric Science, University of Miami, 4600 Rickenbacker Causeway, Miami, FL 33149-1098.
E-mail: jmartinez@rsmas.miami.edu

DOI: 10.1175/JTECH-D-13-00022.1

such as the CODAR SeaSonde (SS). Phased arrays use multiple receive antennas and resolve bearing by beamforming (BF) techniques, where the element-to-element relative phase and gain differences are applied in software to form a beam that can be steered across the radar footprint (Gurgel et al. 1999a,b). By contrast, compact directional antennas, employ direction-finding (DF) techniques, where bearings are resolved in software by fitting the data from all elements in the receive array (two cross loops and a collocated vertical element for SS) to either a measured or modeled antenna response function consisting of relative phase and gain versus bearing. DF processing for the SS employs the Multiple Signal Classification (MUSIC) algorithm (Schmidt 1986) to resolve the direction of arrival for radial surface currents (Barrick et al. 1977; Lipa and Barrick 1983; Barrick and Lipa 1986, 1997; De Paolo and Terrill 2007a,b). It should be noted that phased arrays may also use DF techniques (Teague and Laws 1998; Sentchev et al. 2013), although this is not currently a standard practice, and not addressed herein. Both HF radar types have been extensively tested and evaluated over the years in differing venues. The HF radar–derived surface currents have been compared to various types of in situ measurement platforms (Frisch and Weber 1980; Holbrook and Frisch 1981; Janopaul et al. 1982; Prandle 1987; Paduan and Rosenfeld 1996; Shay et al. 1995, 2002, 2007; Chapman et al. 1997; Essen et al. 2000; Emery et al. 2004; Ohlmann et al. 2007). These comparisons were generally favorable in their assessment of HF radars' capability for resolving radial and combined vector–surface currents.

In the eventual build out of the U.S. HF Radar Network (Paduan et al. 2004) by the U.S. Integrated Ocean Observing System (U.S. IOOS)-certified regional associations, radial current data will have to be combined between DF and BF approaches in some areas (e.g., Shay et al. 2008) to form surface current vectors. Central to the national network, inherent uncertainties in the radial and vector currents must be determined either through the measurement itself or the physical process the HF radar is attempting to resolve (Graber et al. 1997). To assess the impact of combining both DF and BF techniques, a pair of 12.6-MHz direction-finding SS radar units were deployed along the southern end of a WERA domain during a 10-day period in April 2005 by the National Oceanic and Atmospheric Administration's (NOAA) Center for Operational Oceanographic Products and Services (CO-OPS). As shown in Fig. 1, the fairly significant overlap of the grids included an upward-looking acoustic Doppler current profiler (ADCP) (Parks et al. 2009), where the first reliable bin was 14 m below the water surface. The WERAs were transmitting at 16.04 MHz to monitor the Florida Current (FC), including the eddy field along its western flank. These sites have measured near-real-time surface currents over a range of 80–100 km at ~1-km grid spacing in the Florida Straits since July 2004 as part of Southeast Coastal Ocean Observing System Regional Association (SECOORA) and its predecessor, the Southeast Coastal Ocean Observing System. The specifications of both systems are listed in Table 1. Simultaneous measurements from SS, WERA, and the ADCP provided a unique opportunity to test the concept of interoperability between differing radars benchmarked by bottom-mounted ADCP measurements.

2. South Florida ocean circulation

The coastal ocean shelf in south Florida is characterized by shallow and variable topography, where currents are highly variable and respond to forcing at different temporal and spatial scales by winds, tides, internal waves, and the very energetic offshore FC system. The FC is an oceanic regime characterized by large horizontal current shears, with FC intrusion lobelike structures and multiple-scale vortices; these energetic vorticity regimes are up to $4f$ (where f is the local Coriolis parameter) (Peters et al. 2002). The scale of FC perturbations varies along the south Florida coastal ocean from slow-moving mesoscale gyres to faster-moving spin-off eddies, and smaller submesoscale vortices with strong horizontal shear (Lee and Williams 1988; Shay et al. 1998; Haus et al. 2000; Shay et al. 2000).

At the largest scales, the FC has seasonal transport fluctuations due to wind climate changes (Lee and Williams 1988) and gyres with spatial scales of hundreds of kilometers and temporal scales of weeks to months that are topographically linked (Lee et al. 1992). Meanders and waves moving along the inshore edge of the FC can cause offshore displacement of the inshore edge off the upper Florida Keys by up to 30 km (Haus et al. 2000). Many of these processes have temporal scales of 3–7-day periods; these fluctuations force trap and advert a spectrum of transient features such as submesoscales vortices and internal waves that have an impact on mixing between differing water masses (Shay et al. 1998). The FC and its highly variable processes intermittently intrude across the shelf break. The FC, constrained by the Strait of Florida, flows principally northward with velocities exceeding $2\,\mathrm{m\,s^{-1}}$ at the surface at times (Peters et al. 2002; Martinez-Pedraja et al. 2004; Parks et al. 2009). These currents follow the steep bottom terrain along the shelf break, which separates the deep ocean from the coastal flow regimes (Peters et al. 2002).

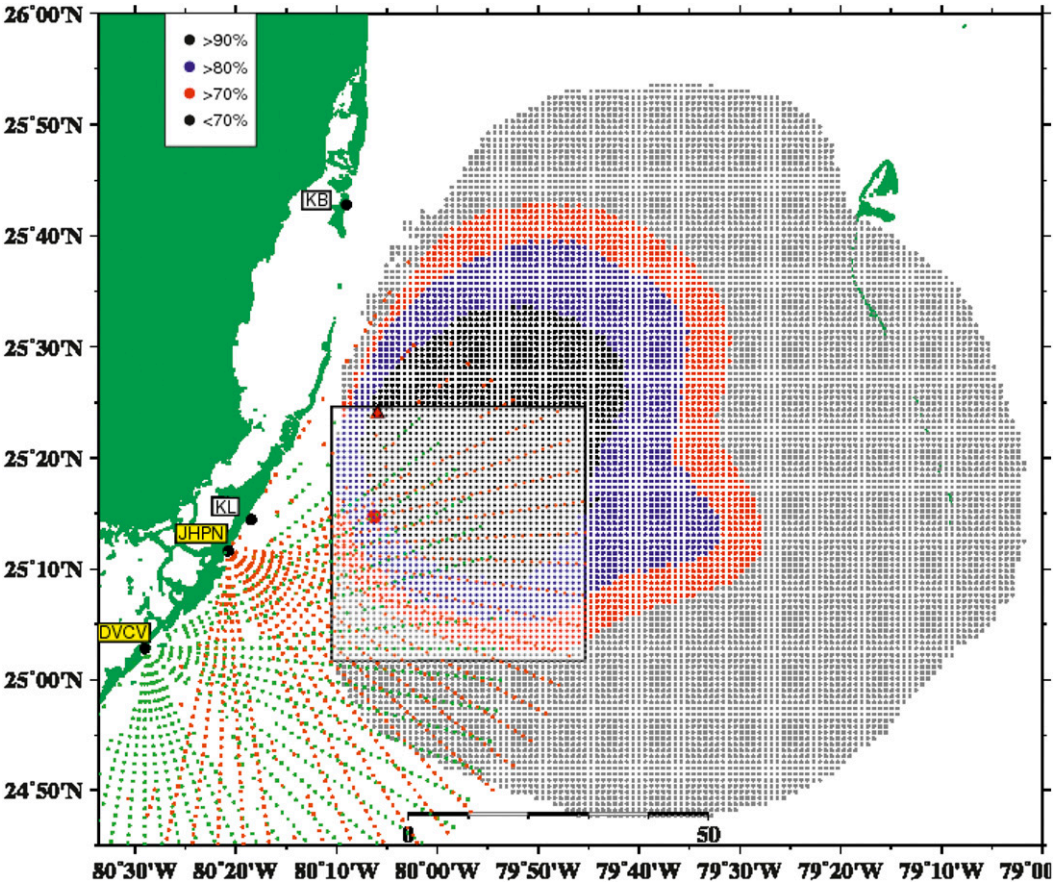

FIG. 1. WERA grid with percentages of vector data and radial coverage relative to the radial grids from the SS measurements from 0200 UTC 16 Apr to 2300 UTC 23 Apr 2005. Radial comparisons were made between the WERA-KL site and the SS-JHPN site located a few kilometers south. ADCP is shown as a red triangle; the cell in which radial comparisons between WERA-KL and SS-JHPN were made is shown as a red circle.

Subtidal nearshore currents along the Florida Keys are influenced by both wind stress and Florida Current fluctuations (Lee et al. 1992).

3. Experimental design

a. Radial current accuracy

The frequency (v_b) of the backscattered signal due to Bragg resonant waves traveling along a nonmoving ocean surface is given by the expression

$$v_b = \pm\sqrt{\frac{gv_r}{\pi(c_0)}}, \tag{1}$$

where g is the acceleration due to gravity ($9.81\,\mathrm{m\,s^{-1}}$), v_r is the radar frequency, and c_0 is the speed of light ($2.9979\times10^8\,\mathrm{m\,s^{-1}}$). Positive and negative Doppler shifts can be observed because of advancing and receding waves, respectively. A superposed surface current both shifts both Bragg peaks into the same direction and causes a frequency shift off the Bragg frequency of

$$\Delta v = \frac{2V_{\mathrm{cr}}v_r}{c_0}, \tag{2}$$

where V_{cr} is the radial component of the current along the look direction of the radar. By measuring Δv, the

TABLE 1. Specifications of SS and WERA HF radars used in this 10-day interoperability study in the Florida Straits.

System characteristics	SS	WERA
Frequency (MHz)	12.60	16.05
Transmit power (W)	30	40
Bragg wavelength (m)	12	9.4
Measurement depth (m)	0.9	0.7
Range (km)	80	80
Resolution (km)	1.3	0.6–2.4
Integration time (min)	60	10
Azimuth resolution (°)	2	2
Radial component ($\mathrm{cm\,s^{-1}}$)	4	2

radial current V_{cr} can be calculated. In the Doppler spectrum, one of the Bragg peaks will be shifted to direct current (DC) when the radial current reaches the speed of the Bragg resonant waves, which is $V_{cr} = 3.8\,\mathrm{m\,s^{-1}}$ for the 16.04-MHz radar frequency.

For DF the resolution of bearing angles with MUSIC processing is complicated; that is, the bearing resolution for a distributed target like the ocean surface is considered an uncertainty in the MUSIC-bearing solution limited by the covariance of signals between the collocated antennas and the Gaussian noise that is inherent in the received sea echo itself. While the azimuthal antenna pattern can be resolved to 1° or better, typical azimuthal uncertainties for sea surface scatter and near-ideal patterns are between 5° and 10° based on azimuthal ambiguities between nearby bearings. More severely distorted antenna patterns can cause larger local bearing uncertainties (de Paolo and Terrill 2007a,b).

In the case of BF mode, n samples of the radial current velocity r_i are taken from the surrounding of the two first-order Bragg peaks. If the Doppler spectrum consists of N_f spectral lines, then the Bragg peaks of $\pm(N_f/64)$ lines are used, so $n = (N_f/16) + 2$. In these calculations, the signal-to-noise ratio [SNR(i)] of each spectral line is used as a weighting factor. Following the center-of-mass approach, the average radial current (r) is

$$\bar{r} = \frac{\sum_{i=1}^{n} r(i)\mathrm{SNR}(i)}{\sum_{i=1}^{n} \mathrm{SNR}(i)} \tag{3}$$

and its variance is

$$r_\sigma^2 = \frac{\sum_{i=1}^{n} r^2(i)\mathrm{SNR}(i)}{\sum_{i=1}^{n} \mathrm{SNR}(i)} - \bar{r}^2. \tag{4}$$

This variance includes measurement errors as well as temporal current variation due to oceanic effects (e.g., horizontal shears in the vector currents). A systematic error or bias is not revealed by this approach. The accuracy is given by

$$r_{\mathrm{acc}} = r_\sigma \sqrt{n^{-1}}. \tag{5}$$

Radial current accuracy is thus estimated by accounting for signal strength and horizontal variations (i.e., shear) within a grid cell for each sample interval. The methodology utilizes the current velocity variance to estimate the accuracy of the radial current measurement. The magnitude of the radial current accuracy is combined through the sum of the squares from each sample ($r_{\mathrm{acc}}^2 + r_{\mathrm{acc}}^2$) and then time averaged over the appropriate intervals. Radial accuracy for the WERA Key Largo, Florida (KL), site is shown (Fig. 2a) from September 2004 through June 2005 within the domain-receiving data with radial accuracies of $5\,\mathrm{cm\,s^{-1}}$ or better at least 70% of the time. Within this region, radial current accuracy ranged from 2 to $4\,\mathrm{cm\,s^{-1}}$, suggestive of quality radial current measurements.

b. Range resolution

Both systems used in this experiment utilize frequency-modulated continuous wave (FMCW) waveforms to resolve range, which divides the coverage areas into concentric circular arcs called range cells. The range resolution, or range cell size, for FMCW systems is

$$\partial R = c(2B)^{-1}, \tag{6}$$

where B is the swept bandwidth of the transmitter pulse and c is the speed of the light ($3 \times 10^6\,\mathrm{m\,s^{-1}}$). The bandwidth, and therefore range resolution limitation, is usually determined by the amount of bandwidth allowed by frequency licensing authorities. In addition, resolution may be lost if a window function is used in range processing. For WERA, which does not pulse the transmit signal, a four-term Blackman–Harris window is required in range processing to reduce the large echoes in early range cells to prevent aliasing in farther ranges with weaker Bragg echoes. This has the effect of reducing resolution such that adjacent range cells overlap approximately 50% in the far field (Harris 1978). For SS, which uses a pulsed, gated FMCW waveform, a Hanning window (Otnes and Enochson 1978) is used in range processing, which also reduces resolution such that adjacent range cells overlap by approximately 15% (Harris 1978). In both cases, though, the range increment remains the same as windowless range processing.

c. Azimuthal resolution

The two techniques of azimuthal resolution that will be discussed are DF and BF. In both cases it is assumed that the transmit antenna is omnidirectional or slightly directed toward the sea (Gurgel et al. 1999b).

1) SEASONDE

The SS utilizes a three-element crossed-loop/monopole receive antenna along with a variant of the MUSIC algorithm (Schmidt 1986) to infer the bearing of the incoming radar return. The DF approach makes use of the amplitude and phase characteristics of a signal on each of three elements on the receive antenna as a function

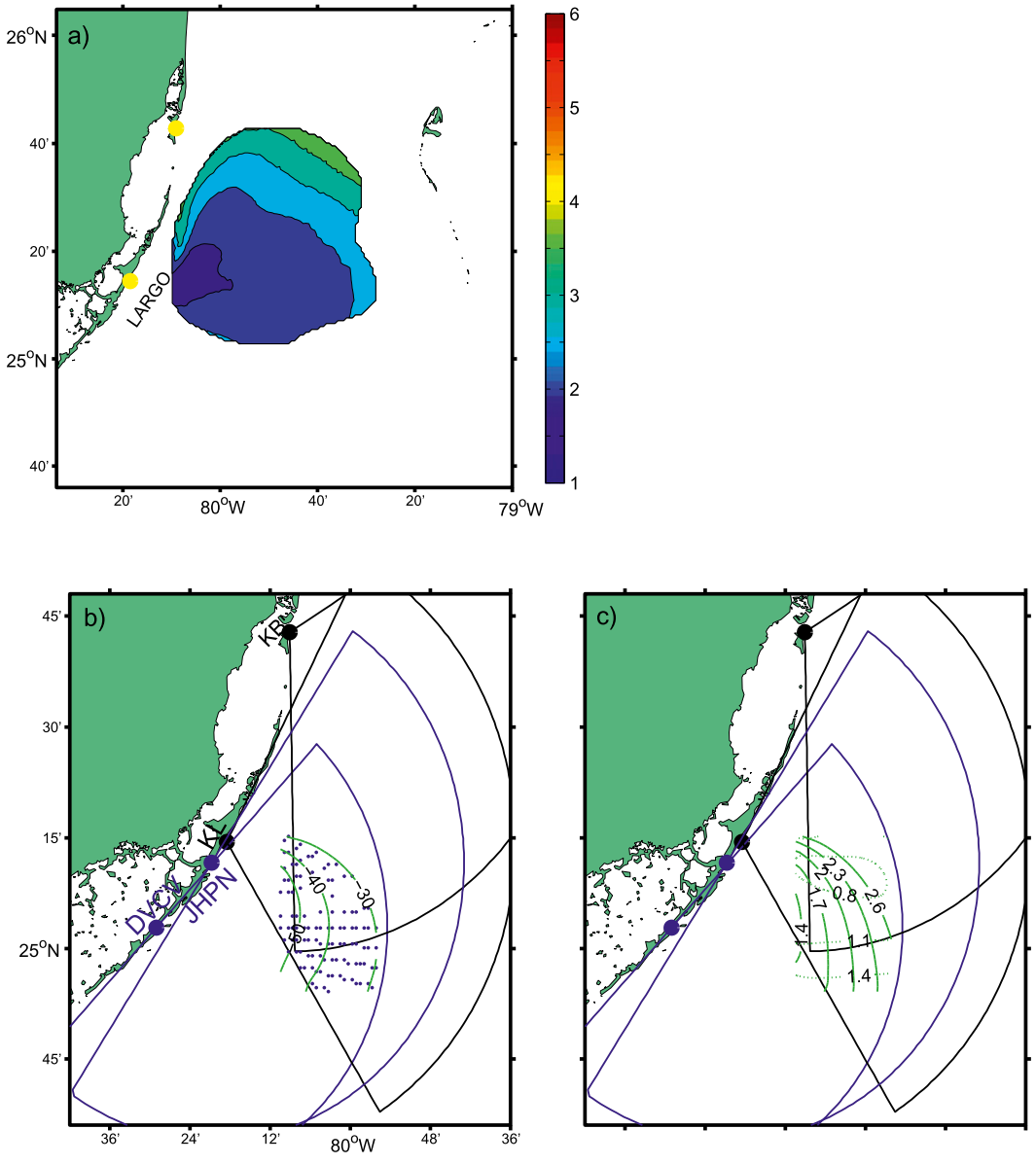

FIG. 2. (a) Mean radial accuracy within the domain receiving data with radial accuracies of 5 cm s^{-1} or better at least 70% of the time from September 2004 through June 2005. (b) The 108 common cells and the intersection angles (°). (c) GDOP relative to the common cells between WERA-KL and SS-DVCV data. The contour interval for the intersection angle is 10°, and the nondimensional GDOP is in 0.3 increments. WERA–SS vector grid is represented by blue dots in (b).

of angle. In DF mode the azimuthal increment is typically 5° (Paduan et al. 2006). The DF algorithm assigns current magnitudes to radar azimuth. For a system with N antenna elements, each Doppler bin containing a valid first-order Bragg echo can produce up to $N - 1$ estimates of the bearing for the radial velocity corresponding to that Doppler shift. For each range cell, SS can produce up to four bearing solutions for each Doppler bin given two Bragg peaks present and up to two bearing solutions given a single Bragg peak. SS software reports the median of the radial currents that are assigned to each azimuthal increment (Laws et al. 2000, 2011). DF algorithms cannot always resolve radial current vectors for all angular directions in a given range cell, which is unique to the SS type of HF radars (see Paduan and Rosenfeld 1996).

The SS carrier frequency was 12.6 MHz. In the configuration for this experiment, unaveraged Doppler spectra were obtained every 256 s and averaged over 10 min and then processed to obtain radial current

estimates. The average of radial current estimates from seven 10-min spectra form the final radial current estimates reported at hourly intervals.

2) WERA

At a transmission frequency of 16.04 MHz corresponding to Bragg wavelengths of 9.4 m, the WERA system requires a 126-m baseline distance for a 16-element phased array. When operating with a linear array, BF in the time domain is used for azimuthal resolution. As the number of receiver antenna elements increase, azimuthal resolution improves (Teague et al. 2001). Beamwidth is a function of the radar wavelength divided by the length of a phased array, which is 7.5° at broadside for the 16-element array, increasing to 15° at a steering angle of 60° off the broadsides of the array. The transmitter is arranged to encompass a 120° swath. Fourier analysis of the beam-formed time series yields the Doppler spectrum for a range cell on the sea surface, defined on a fixed grid. The peak frequency of the Doppler spectrum determines the current speed, and the broadness of the spectrum allows one to estimate the standard deviation of the current speed. The standard radial output is not reported on a polar grid, but a Cartesian grid. After range processing/sorting, the beam is formed in the direction of each Cartesian grid point and the two nearest range cells are interpolated to produce a solution matching the Cartesian grid point.

For this experiment, the WERA carrier frequency was 16.04 MHz, the sampling interval was 0.26 s, and measurements of 9-min duration were made every 20 min for a total of 2048 samples.

d. Vector current accuracy

Because the frequency of the transmitted signal and the corresponding Bragg wavelength set the integrating depth of the measurement (Stewart and Joy 1974), combining radials from two systems requires careful mapping onto a common grid (Teague et al. 2001). The depth difference between these two frequencies (12.6 and 16.045 MHz) following $\lambda_{radar}/8\pi$ (Stewart and Joy 1974) is approximately 20 cm (Table 3); this difference was deemed to be inconsequential in combining the radials at the grid points, where the minimum ocean depth is about 100 m. Critical to creating reliable vector current fields from HF radar radial measurements is the intersection angle between the radials emanating from each site. Geometrical limitations are set by the location of the radar sites. This influence of the geometry on the surface current measurement errors is known as the geometric dilution of precision (GDOP), which is a function of the angles of intersection of the radial current measurements (Chapman et al. 1997). This optimal angle lies between 30° and 150° (Shay et al. 2007). Although this constraint can be relaxed somewhat given the configuration, the proof is in how well surface current vectors are resolved in the near and far fields of these radars. Chapman et al. (1997) derived the GDOP for the Cartesian current components based on the radar's mean look direction (α) and the half angle (θ) between intersecting beams. The GDOP is defined as the ratios of (σ_u/σ) and (σ_v/σ) for the variance of the u and v components (positive is east and north), respectively, and σ is the total RMS variance. Radial combinations for this experiment were done between the WERA-KL and SS-DVCV (SS south site) sites because of the quality GDOP as discussed below (Figs. 2b,c). A second aspect in combining radial currents deals with spatial increments (1 vs 3 km). To examine the question of interoperability between BF and DF technologies, radial and vector datasets are combined to form a concurrent time series over a common grid.

TABLE 2. Bearing direction (°) and distances between WERA-KL, SS-JHPN, and the moored ADCP location in the radar domain located at 25°24.04′N, 80°05.92′W as reported in Parks et al. (2009).

Instrument	Bearing (°)	Distance (km)
WERA-KL	40.2	26.8
SS-JHPN	42.8	33.2

4. Measurements

Moored ADCP

From September 2004 to June 2005, a bottom-mounted, upward-looking 300-kHz ADCP was deployed in approximately 100 m of water (Parks et al. 2009). This instrument was deployed inside the WERA domain, with similar bearing to the KL and JHPN (SS north site) sites (Table 2). It was located approximately 0.7 km to the centroid of the nearest WERA cell and 1.1 km from the nearest SS cell. The ADCP measured currents at 2-m vertical intervals at 30-min temporal intervals (Table 3) from 14 to 86 m. Errors commonly occur in bottom-mounted ADCP measurements near the surface because of sidelobe interference (Johns 1988). Current signals from near-surface bins were analyzed for possible noise interference over the 9-month record. Consequently, the bin at 14-m depth was utilized as the bin closest to the surface that was not susceptive to sidelobe contamination. This ensures that high-quality samples are used for these comparisons. Bin-to-bin RMS differences, estimated for the ADCP over the 8-day time series, were less than 2 cm s^{-1} in the upper 50 m of the water column for the u and v components, suggestive of quality ADCP measurements (Parks et al. 2009).

TABLE 3. Positions, sensor depths (m), and sampling intervals (min) for ADCP, WERA, and SS cells with those closest to the ADCP cell and measurements were in an area where the water depth was approximately 100 m.

Instrument	Lat (°N)	Lon (°W)	Sensor depth (m)	Sampling (min)
ADCP	25°24.04	80°05.92	14	30
WERA-KL (ADCP cell)	25°23.84	80°06.27	0.7	20
WERA-KL	25°15.20	80°05.67	0.7	20
SS-JHPN (ADCP cell)	25°23.72	80°06.48	0.9	60
SS-JHPN	25°14.70	80°06.27	0.9	60

5. Sensors comparisons

It was useful to compare how WERA, SeaSonde, and ADCP differ in their characterization of the actual current field.

Radial and vector SS data used for the comparisons were corrected for the measured antenna pattern following Kohut and Glenn (2003). WERA time series of radial and vector surface currents were acquired at 20-min intervals, whereas SS time series were acquired at 1-h intervals. To facilitate direct comparisons between the radial velocities of SS-JHPN and WERA-KL, all data were smoothed using a three-point Hanning window (Otnes and Enochson 1978) and the WERA-KL data were subsampled at 1-h intervals to compare with SS-JHPN because of their spatial proximity and similar bearings and distances to the ADCP.

a. Time-averaged radial and vector currents

Mean radial current maps from an 8-day average for WERA-KL and SS-JHPN are shown in Figs. 3a and 3b (top panel). Maximum radial values ranging between 50 and 60 cm s^{-1} were observed from both radar sites in the north-northeast part of the subdomain. WERA-KL radials show greater values (~10 cm s^{-1}) than SS-JHPN in the southwestern corner of their subdomain, which is out of the area of high-quality WERA data based on GDOP

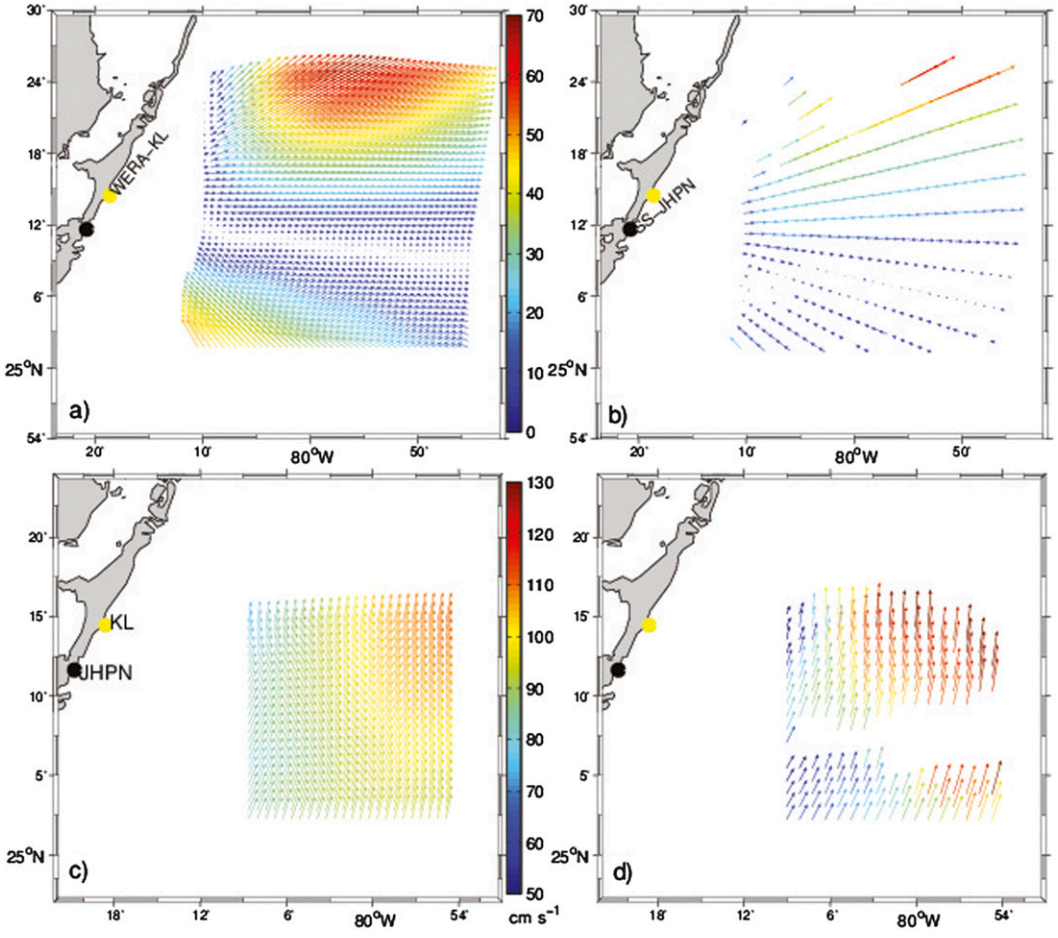

FIG. 3. Eight-day averaged radial currents (cm s^{-1}) for (a) WERA-KL and (b) SS-JHPN, and vector currents for (c) WERA (KL–KB) and (d) SS (JHPN–DVCV) from concurrent records in April 2005.

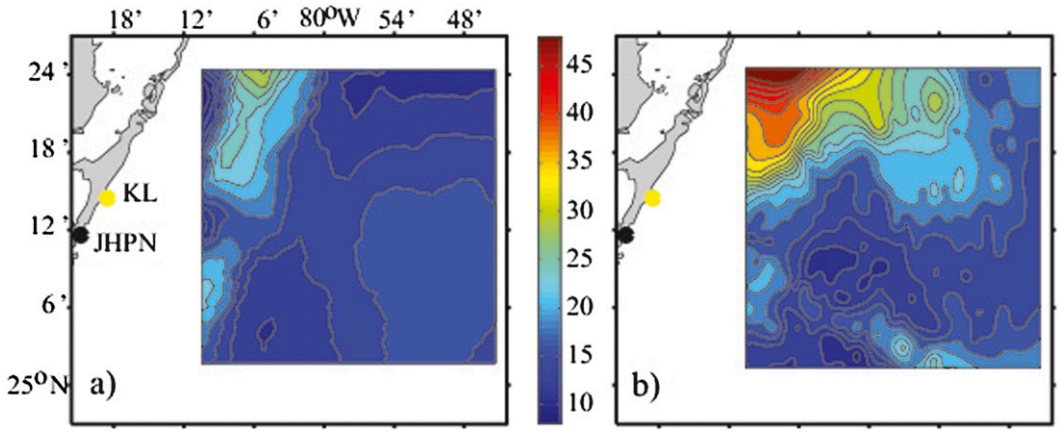

FIG. 4. Standard deviations (cm s^{-1}) in the (a) WERA-KL and (b) SS-JHPN radial currents.

consideration (Fig. 2a). The 8-day averaged vector currents during the same period of time were obtained by combining the WERA [Key Biscayne and Key Largo, Florida (KB)–KL] and SS (JHPN-DVCV) sites over the common subdomain of each HF radar (Figs. 3c,d). Both sets of HF radar data show a similar current pattern with the usual surface current variability along the western flank of the FC. Surface velocities ranged between 70 and 110 cm s^{-1} over the WERA footprint and between 50 and 120 cm s^{-1} over the SS domain. In addition to measurement uncertainties, these velocity differences may be due to different temporal and spatial averaging performed by the systems. (Essen et al. 2000).

To understand the distribution of the radial current variability for both SS and WERA, the standard deviations of the radial currents were estimated from the time series. The standard deviations of the radial currents derived from WERA-KL (Fig. 4a) and SS-JHPN (Fig. 4b) differed by a factor between 2 and 4 in the northwestern corner of the subdomain. Over the remainder of the common footprint, the standard deviations are similar. For the WERA-KL radial currents, the standard deviation reached a maximum of 30 cm s^{-1} in a small northwestern area, whereas values were less than 15 cm s^{-1} over the remainder of the domain. The standard deviation in the SS-JHPN radial currents was a maximum of 45 cm s^{-1} in the northwestern corner of the domain; SS radials in this area of the domain were adversely affected by the interaction with the upper Keys land surfaces. Over the central and lower portions of the domain, standard deviations decreased to less than 20 cm s^{-1}.

b. *Time series*

Surface winds were compared to radial surface and subsurface currents at the ADCP site (Fig. 5). Hourly wind speed and direction were obtained for the same period of time from the National Data Buoy Center (NDBC) Coastal-Marine Automated Network (C-MAN) station located at Fowey Rocks, Florida (25°35.4′N, 80°6.0′W), just inshore of both radar domains. Wind magnitude and direction data were converted to the 10-m reference level (Fairall et al. 1996). Wind velocities ranged from 10 m s^{-1} during frontal passage in the early part of the time series toward the south and then steadily decreased; during that time the winds shifted direction to the southwest, reversing directions by day of year 112. The associated surface friction velocity (u_*) reflected a gradual decrease from 0.5 to 0.1 m s^{-1} as the front moved through the area in Fig. 5b. Of central importance here is the comparison of HF radar–derived surface currents and the subsurface current radials from the ADCP. The frontal passage in the early part of the record forced subsurface flows of 50 cm s^{-1} in the surface layer and 60 cm s^{-1} at 14 m (Fig. 5c). Subsequently, the radial currents between the surface and subsurface levels were similar at the WERA cell 0.7 km from the ADCP site (θ = 40.2°). Comparison at the ADCP site indicates good agreement using radial currents from WERA-KL, by contrast radial currents from SS-JHPN (θ = 42.8°) revealed large differences at the ADCP, partly because of the interaction with the land as noted above. Consequently, comparisons between radar radials were made at a less obstructed location (red circle in Fig. 1) as shown in Fig. 5d. Here, there is marked agreement between WERA-KL and SS-JHPN radial currents. The scatter in these signals is reflected in Figs. 5e and 5f. The slope of the regression line between the WERA-KL and the ADCP was 1.3 with a bias of −12 cm s^{-1}. However if we remove the frontal passage period, then the slope decreased to levels of ~1 as reported by Parks et al. (2009); that is, during that frontal

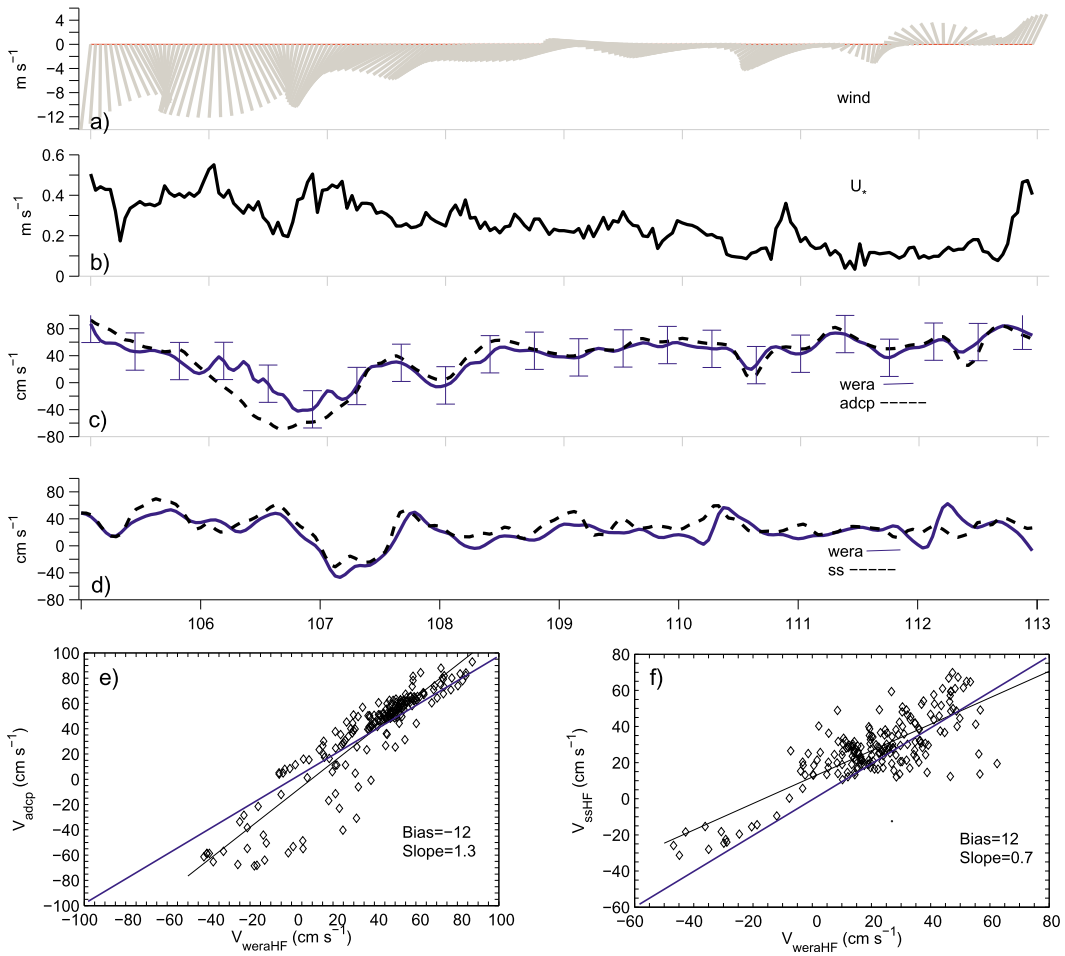

FIG. 5. Time series of (a) wind vectors and (b) surface frictional velocity from Fowey Rocks C-MAN station ($m\,s^{-1}$); radial currents from (c) WERA-KL and ADCP and (d) WERA-KL and SS-JHPN, and scatter diagrams with observed (black) and ideal slopes (blue); and (e) WERA-KL and ADCP and (f) WERA-KL and SS-DVCV [as in (c),(d)].

passage period, the subsurface radial current was larger than the surface current, which seems counterintuitive. However, given the significant cross-shelf exchanges that often occur along the western flank of the FC, such differences have been observed previously in concurrent HF radar and ADCP measurements (Shay et al. 2002). The scatterplot between WERA and SS radial currents suggests a $12\,cm\,s^{-1}$ bias and a slope of 0.7. The different temporal averaging and the interpolation onto a common time base may explain part of these differences. Given the levels of variability in this region, the results do point to coherence between the two signals from both HF radars in resolving the surface current field.

Another statistical measure of the correlation between two differing vector measurements is the complex correlation coefficient and phase angle (Kundu 1976). Radial velocities at the ADCP were used to estimate the complex correlation coefficients averaged over the time series at each of the overlapping 108 cells (WERA-KL and SS-JHPN) (Fig. 6). Correlation coefficients followed the orientation of the isobaths for both radar sites with a maximum of 1 for WERA-KL at the mooring location (Fig. 6a). Correlation coefficients decreased to less than 0.4 in the remainder of the domain. For SS-JHPN a maximum of 0.8 at the ADCP site following the orientation of the same isobaths (Fig. 6b). Correlation coefficients decreased to less than 0.4 over the rest of the domain. This observed decrease in their respective correlation values for both radars is presumably due to the significant cross-shelf current variability. As noted, this is a coastal ocean subject to large relative vorticity change across the shelf break associated with FC intrusion that force submesoscale variations in the surface currents with large cross-shelf gradients (Peters et al. 2002).

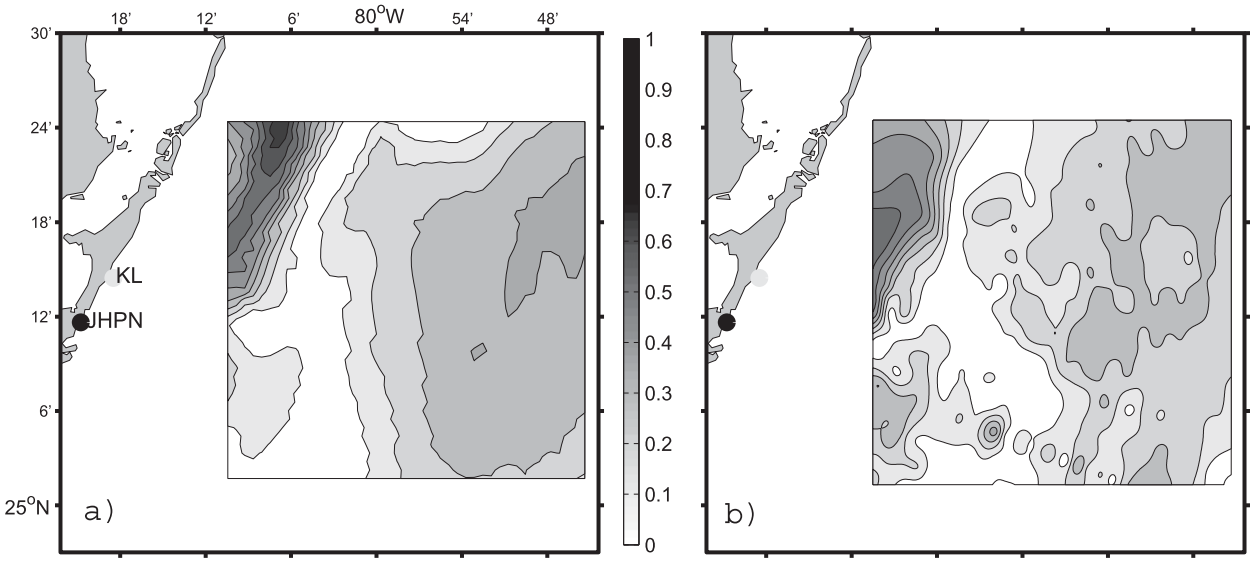

FIG. 6. Complex correlation coefficient for (a) WERA and (b) SS relative to the currents at the ADCP cell as in Table 3.

6. Interoperability

Considering the ideal baseline separation between radars, based in its frequency transmissions, WERA-KL and SS-DVCV (28-km distance) were the sites selected for the interoperability experiment between the two technologies. Additionally, the WERA-KL site was used in the previous comparisons and radials overlapping the SS domain. Thus, we use 108 common cells as per Fig. 2. As the combined radial vectors deviate from orthogonality, the potential error in the total vectors tends to increase. GDOP is a tool to be used as a constraint to the HF radar measurement domain; it characterizes the effect of the geometry of the coupled radars system on the measurement and position determination errors. A low GDOP correspond to an optimal geometric configuration of radar stations. To construct reliable vector current fields by combining the radials from the WERA and SS sites in this new domain, the intersection angles are limited here to 30°–150° (see Fig. 2b), encompassing a small region. Here, the GDOP ranges from 0.8 to 2.6 (Fig. 2c), suggestive of quality data.

A uniform grid was produced over the study's domain using the coordinates of WERA and SS cells. The represented surface was interpolated using a triangle-based cubic interpolation method based on a *Delaunay triangulation* of the radial current data (Watson and Phillip 1984). The average surface currents are shown in Fig. 7, for the 8-day time series on the produced grid, from WERA (Fig. 7a), SS (Fig. 7b), and the combined WERA–SS (KL–DVCV) (Fig. 7c) sites. Mean surface currents exhibited a similar structure, suggesting good agreement in direction, with some differences in velocity, mainly at the eastern part of the domain, where surface current variability is greater because of the core of the FC.

Based on the 108 common cells, the means and standard deviations are given in Table 4 for the time series. Relative to SS only, the difference in the mean v components showed is $\sim 12\,\mathrm{cm\,s^{-1}}$ with respect to WERA and WERA–SS. The largest value for the u component of the standard deviation was $7.2\,\mathrm{cm\,s^{-1}}$ for WERA, whereas the v component showed a maximum value of $14.8\,\mathrm{cm\,s^{-1}}$ for SS. RMS differences (Table 5) between the three systems (BF–BF, DF–DF, and BF–DF) had a maximum value for the v component of $23.2\,\mathrm{cm\,s^{-1}}$ between WERA and SS and $19.4\,\mathrm{cm\,s^{-1}}$ between WERA–SS and SS. The standard deviation of the u and v components of the surface currents are shown in Fig. 8. The standard deviation in the u component for WERA (Fig. 8a) tends to increase into the southwestern corner of the domain as noted, but it shows similar values around the region for SS (Fig. 8c) and relatively less for WERA–SS (Fig. 8e). The v component shows a general increase in the current structure toward the north as well as east-northeast for the SS (Fig. 8d) domain, and slightly into the northeastern corner and central-east of the WERA–SS (Fig. 8f); in the WERA (Fig. 8b) domain, the v component shows a slight increase into the south. With such a short time period (8 days), we are unable to conclude whether this variability in the u and v components is related to smaller-scale motions, or both submesoscale and larger mesoscale features. In the case of WERA, the standard deviation increase into the southwest corner of the domain is possibly an artifact of

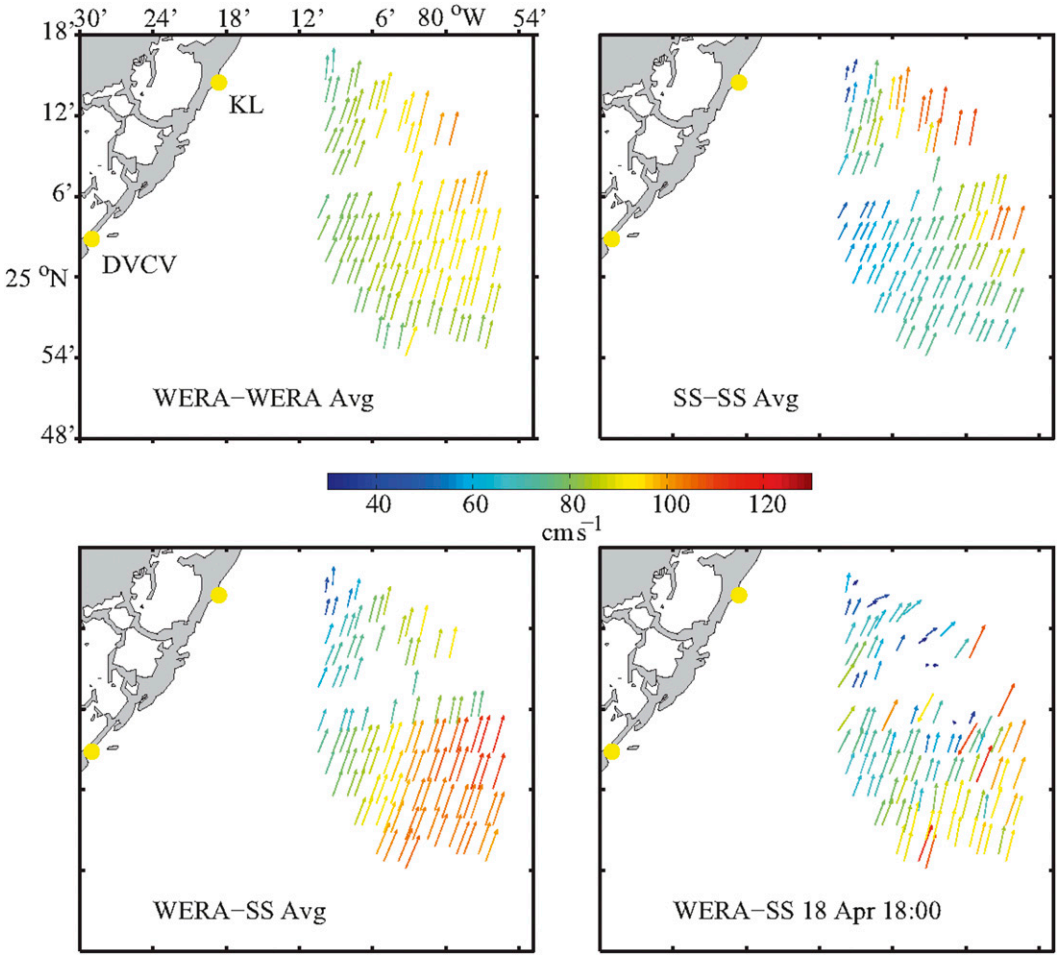

FIG. 7. Eight-day average of (a) dual WERA stations, (b) dual SS stations, (c) WERA-KL and SS-DVCV, and (d) snapshot of surface currents from WERA-KL and SS-DVCV from 1800 UTC 18 Apr 2005.

a decrease in radial current accuracy outside of the 70% region (Fig. 1) (Parks et al. 2009).

7. Summary and concluding remarks

During a period of eight days in April 2005, surface-current measurements of two pairs of HF radar systems—WERA in beam-forming mode and SS with the direction-finding technique transmitting at 16.045 and 12.6 MHz, respectively—were compared and combined. HF-measured current velocities were compared with subsurface current measurements (14-m depth) from an ADCP.

Current velocities comparisons between the different HF radars—WERA, SS, and WERA–SS—revealed RMS differences of 3–23 cm s^{-1}.

TABLE 4. Mean and standard deviation for u and v current components of the total surface vector current averaged over all 108 common cells.

Component	Platform	Mean (cm s^{-1})	Std (cm s^{-1})
u	WERA	24.3	7.2
	SS	24.6	3.0
	WERA–SS	27.1	3.1
v	WERA	82.7	5.0
	SS	70.6	14.8
	WERA–SS	83.5	10.3

TABLE 5. RMS differences (cm s^{-1}) for u and v components relative to WERA (KB–KL) for SS (JHPN–DVCV) only and combined WERA (KL)–SS (DVCV) from the 108 common overlapping cells.

Component	Platform	SS (cm s^{-1})	WERA–SS (cm s^{-1})
u	WERA	7.7	5.1
	SS		2.6
v	WERA	23.2	3.8
	SS		19.4

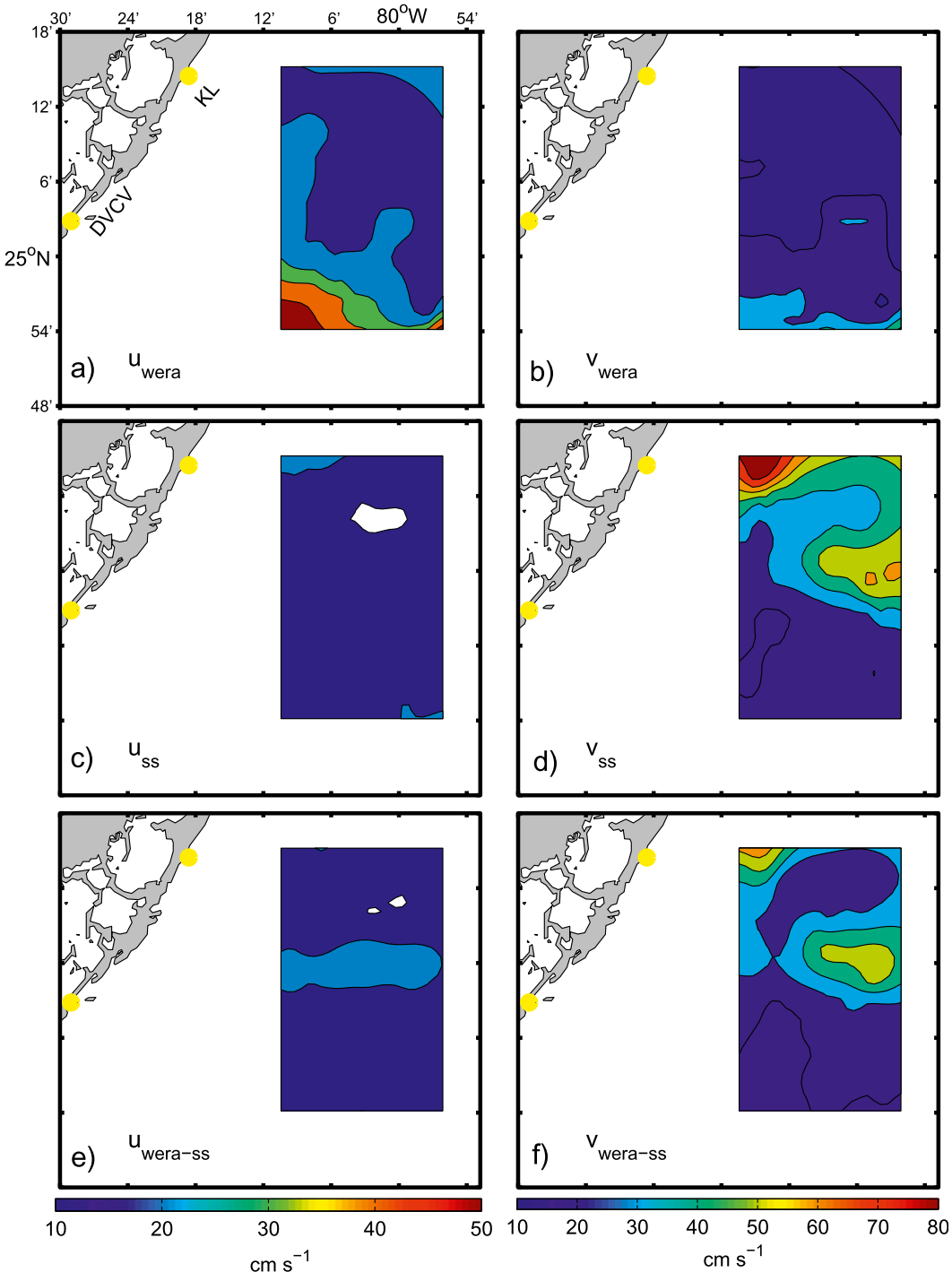

FIG. 8. Standard deviations (cm s^{-1}) for the (left) u and (right) v components for (a),(b) WERA; (c),(d) SS; and (e),(f) WERA–SS sites' vector current over the eight days of measurement period.

In addition to measurement uncertainties, the velocity differences found between the three dual-station radars—WERA (KB–KL), SS (JHPN–DVCV), and WERA–SS (KL–DVCV)—may be due to different spatial and temporal averaging, and the interpolation onto a common time base performed by the systems. Given the high levels of variability in this region, the results points to coherence between the two signals from both radars.

This study shows that radial currents from two differing radars can be realistically combined to form surface vector currents. Longer time series (>8 days) are needed with more overlap to be acquired concurrently with both DF and BF technologies. Based on what was found here, the following are key recommendations:

1) Establish statistics and accuracy limits for the HF radar system to assess performance metrics for all HF radars; and,
2) Develop protocols for the interoperability of diverse HF radar platforms within an operational observing system.

To assess radar performances over broad dynamical ranges with large SNR, interoperability issues must be explored in several venues around U.S. coastlines in support of the U.S. HF Radar Network. Such studies would also provide the error covariance matrix, which is needed for data assimilation studies.

This particular region has a high dynamical range of features and represents substantial measurement challenges for HF radar systems at high spatial and temporal resolution. Understanding these interoperability conditions will provide a significant contribution to the development of a robust nationwide Regional Coastal Ocean Observing System (RCOOS) that includes various HF radar systems.

Acknowledgments. LKS and Team WERA (Jodi Brewster, Thomas Cook, Jorge Martinez-Pedraja, Matthew Archer, Brian Haus, and Brad Parks) were supported by ONR through the SEACOOS program (Grant N00014-02-1-0972) administered by the University of North Carolina General Administration and now through the NOAA IOOS SECOORA Grant IOOS.11(033)UM.LSOBS.2. We are thankful for the continued efforts of Jodi Brewster, Brad Parks, and Matthew Archer. We appreciate the reviewer's thorough comments, insights, and editorial suggestions, aimed at improving the manuscript. The moored ADCP in the Florida Straits was provided by Bill Johns and the OTECH staff at UM. Mark Bushnell, Karen Grissom, and Jennifer Dussault provided the SS data from the 8-day deployment in south Florida. We thank the following people who have helped us with locations for the radars: Dr. Renate Skinner, Mr. Jim Duquesnel, and Mr. Eric Kiefer from the Florida DEP for our site in the Key Largo Hammock Botanical State Park. Mr. Kevin Kirwan and Mr. Ernest Lynk from Miami-Dade County Parks and Recreation provided space for the site in Crandon Park on Key Biscayne. We thank Thomas Helzel (WERA), and Bruce Nyden, Chad Whelan, and Hector Aguilar (CODAR) for their support of the project.

REFERENCES

Barrick, D. E., and B. J. Lipa, 1986: Correcting for distorted antenna patterns in CODAR ocean surface measurements. *IEEE J. Oceanic Eng.,* **11,** 304–309.

——, and ——, 1997: Evolution of bearing determination in HF current mapping radars. *Oceanography,* **10,** 72–75.

——, M. W. Evans, and B. L. Weber, 1977: Ocean surface currents mapped by radar. *Science,* **198,** 138–144.

Chapman, R. D., L. K. Shay, H. C. Graber, J. B. Edson, A. Karachintsev, C. L. Trump, and D. B. Ross, 1997: On the accuracy of HF radar surface current measurements: Intercomparisons with ship-based sensors. *J. Geophys. Res.,* **102** (C8), 18 737–18 748.

Crombie, D. D., 1955: Doppler spectrum of sea echo at 13.56 Mc./s. *Nature,* **175,** 681–682.

De Paolo, T., and E. Terrill, 2007a: Properties of HF radar compact antenna arrays and their effect on the MUSIC algorithm. Scripps Institution of Oceanography Tech. Rep., 40 pp.

——, and ——, 2007b: Skill assessment of resolving ocean surface current structure using compact-antenna-style HF radar and the MUSIC direction-finding algorithm. *J. Atmos. Oceanic Technol.,* **24,** 1277–1300.

Emery, B. M., L. Washburn, and J. Harlan, 2004: Evaluating radial current measurements from CODAR high-frequency radar with moored current measurements. *J. Atmos. Oceanic Technol.,* **21,** 1259–1271.

Essen, H.-H., K.-W. Gurgel, and T. Schlick, 2000: On the accuracy of current measurements by means of HF radar. *IEEE J. Oceanic Eng.,* **25,** 472–480.

Fairall, C., E. F. Bradley, D. P. Rogers, J. B. Edson, and G. S. Young, 1996: Bulk parameterization of air-sea fluxes for the Tropical Ocean-Global Atmosphere Coupled-Ocean Atmosphere Response Experiment. *J. Geophys. Res.,* **101** (C2), 3747–3764.

Frisch, A. S., and B. L. Weber, 1980: A new technique for measuring tidal currents by using a two-site HF Doppler radar system. *J. Geophys. Res.,* **85** (C1), 485–493.

Graber, H. C., B. K. Haus, R. D. Chapman, and L. K. Shay, 1997: HF radar comparisons with moored estimates of current speed and direction: Expected differences and implications. *J. Geophys. Res.,* **102** (C8), 18 749–18 766.

Gurgel, K.-W., G. Antonischki, H.-H. Essen, and T. Schlick, 1999a: Wellen Radar (WERA): A new ground wave HF radar for remote sensing. *Coastal Eng.,* **37,** 219–234.

——, H.-H. Essen, and S. P. Kingsley, 1999b: High frequency radars: Limitations and recent developments. *Coastal Eng.,* **37,** 201–218.

Harris, F. J., 1978: On the use of windows for harmonic analysis with the discrete Fourier transform. *Proc. IEEE,* **66,** 51–84.

Haus, B. K., J. Wang, J. Rivera, N. Smith, and J. Martinez-Pedraja, 2000: Remote radar measurements of shelf currents off Key Largo. *Estuarine Coastal Shelf Sci.,* **51,** 553–569.

Holbrook, J. R., and A. S. Frisch, 1981: A comparison of near-surface CODAR and VACAM measurements in the Strait of Juan de Fuca, August 1978. *J. Geophys. Res.,* **86** (C11), 10 908–10 912.

Janopaul, M. M., P. Broche, J. C. de Maistre, H. H. Essen, C. Blanchet, G. Grau, and E. Mittelstaedt, 1982: Comparison of measurements of sea currents by HF radar and by conventional means. *Int. J. Remote Sens.,* **3,** 409–422.

Johns, W. E., 1988: Near-surface current measurements in the Gulf Stream using an upward-looking acoustic Doppler current profiler. *J. Atmos. Oceanic Technol.,* **5,** 602–613.

Kohut, J. T., and S. M. Glenn, 2003: Improving HF radar surface current measurements with measured antenna beam patterns. *J. Atmos. Oceanic Technol.,* **20,** 1303–1316.

Kundu, P. K., 1976: Ekman veering observed near the ocean bottom. *J. Phys. Oceanogr.,* **6,** 238–242.

Laws, K. E., D. M. Fernandez, and J. D. Paduan, 2000: Simulation-based evaluations of HF radar ocean current algorithms. *IEEE J. Oceanic Eng.,* **25,** 481–491.

——, J. F. Vesecy, and J. D. Paduan, 2011: Error assessment of HF radar-based ocean current measurements: An error model based on sub-period measurement variance. *2011 IEEE/OES 10th Current, Waves and Turbulence Measurements (CWTM 2011),* IEEE, 70–76.

Lee, T. N., and E. Williams, 1988: Wind-forced transport fluctuations of the Florida current. *J. Phys. Oceanogr.,* **18,** 937–946.

——, C. Rooth, E. Williams, M. Mcgowan, A. Szmant, and M. E. Clarke, 1992: Influence of Florida current gyres and wind-driven circulation on transport of larvae and recruitment in the Florida Keys coral reefs. *Cont. Shelf Res.,* **12,** 971–1002.

Lipa, B. J., and D. E. Barrick, 1983: Least-squares methods for the extraction of surface currents from CODAR crossed loop data: Application at ARSLOE. *IEEE J. Oceanic Eng.,* **8,** 226–253.

Martinez-Pedraja, J. J., L. K. Shay, and T. M. Cook, and B. K. Haus, 2004: Very-high frequency surface current measurement along the inshore boundary of the Florida current during NRL-2001. Rosenstiel School of Marine and Atmospheric Sciences Tech. Rep. RSMAS 2004-03, 34 pp.

Ohlmann, J. C., P. F. White, L. Washburn, E. Terrill, B. Emery, and M. Otero, 2007: Interpretation of coastal HF radar–derived surface currents with high-resolution drifter data. *J. Atmos. Oceanic Technol.,* **24,** 666–680.

Otnes, R. K., and L. Enochson, 1978: *Applied Time Series Analysis: Basic Techniques.* Vol. 1. John Wiley, 449 pp.

Paduan, J. D., and L. K. Rosenfeld, 1996: Remotely sensed surface currents in Monterey Bay from shore-based HF radar (Coastal Ocean Dynamics Application Radar). *J. Geophys. Res.,* **101** (C9), 20 669–20 686.

——, and H. C. Graber, 1997: Introduction to high-frequency radar: Reality and myth. *Oceanography,* **10,** 36–39.

——, and Coauthors, 2004: Surface current mapping in U.S. coastal waters: Implementation of a national system. Ocean.US Rep., 22 pp.

——, K. C. Kim, M. S. Cook, and F. P. Chavez, 2006: Calibration and validation of direction-finding high-frequency radar ocean surface current observations. *IEEE J. Oceanic Eng.,* **31,** 862–875.

Parks, A. B., L. K. Shay, W. E. Johns, J. Martinez-Pedraja, and K.-W. Gurgel, 2009: HF radar observations of small-scale surface current variability in the Straits of Florida. *J. Geophys. Res.,* **114,** C08002, doi:10.1029/2008JC005025.

Peters, H., L. K. Shay, A. J. Mariano, and T. M. Cook, 2002: Current variability on a narrow shelf with large ambient vorticity. *J. Geophys. Res.* **107,** 3087, doi:10.1029/2001JC000813.

Prandle, D., 1987: The fine-structure of nearshore tidal and residual circulations revealed by H. F. radar surface current measurements. *J. Phys. Oceanogr.,* **17,** 231–245.

Schmidt, R., 1986: Multiple emitter location and signal parameter estimation. *IEEE Trans. Antennas Propag.,* **34,** 276–280.

Sentchev, A., P. Forget, Y. Barbin, and M. Yaremchuk, 2013: Surface circulation in the Iroise Sea (W. Brittany) from high resolution HF radar mapping. *J. Mar. Syst.,* **109–110** (Suppl.), S153–S168.

Shay, L. K., H. C. Graber, D. B. Ross, and R. D. Chapman, 1995: Mesoscale ocean surface current structure detected by HF radar. *J. Atmos. Oceanic Technol.,* **12,** 881–900.

——, T. N. Lee, E. J. Williams, H. C. Graber, and C. G. H. Rooth, 1998: Effects of low-frequency current variability on near-inertial submesoscale vortices. *J. Geophys. Res.,* **103** (C9), 18 691–18 714.

——, and Coauthors, 2000: VHF radar detects oceanic submesoscale vortex along Florida coast. *Eos, Trans. Amer. Geophys. Union,* **81,** 209–213, doi:10.1029/00EO00143.

——, T. M. Cook, H. Peters, A. J. Mariano, P. An, A. Soloviev, R. Weisberg, and M. Luther, 2002: Very high frequency radar mapping of surface currents. *IEEE J. Oceanic Eng.,* **27,** 155–169.

——, J. Martinez-Pedraja, T. M. Cook, B. K. Haus, and R. H. Weisberg, 2007: High-frequency radar mapping of surface currents using WERA. *J. Atmos. Oceanic Technol.,* **24,** 484–503.

——, D. Savidge, R. Styles, H. Seim, and R. H. Weisberg, 2008: High-frequency radar observing systems in SEA-COOS: Lessons learned 2002-2007. *J. Mar. Technol. Soc.,* **42,** 55–67.

Stewart, R. H., and J. W. Joy, 1974: HF radio measurements of surface currents. *Deep-Sea Res.,* **21,** 1039–1049.

Teague, C. C., and K. E. Laws, 1998: HF multifrequency ocean-current radar: MUSIC direction finding vs. beam formation. *Wave Propagation and Remote Sensing: Proceedings of the 8th URSI Commission F Triennial Open Symposium,* Universidade de Aveiro, 105–108.

——, J. F. Vesecky, and Z. R. Hallock, 2001: A comparison of multifrequency HF radar and ADCP measurements of near-surface currents during COPE-3. *IEEE J. Oceanic Eng.,* **26,** 399–405.

Watson, D. F., and G. M. Philip, 1984: Triangle based interpolation. *Math. Geol.,* **16,** 779–795.